This is the pre-peer reviewed version of the following article: ChemSusChem, 14, 6, 1595-1601 which has been published in final form at https://doi.org/10.1002/cssc.202002782. This article may be used for non-commercial purposes in accordance with Wiley Terms and Conditions for Use of Self-Archived Versions.

# Push-Pull Electronic Effects in Surface-Active Sites Enhance Electrocatalytic Oxygen Evolution on Transition Metal Oxides

Felipe Andrés Garcés-Pineda,[a] Huu Chuong Nguyën,[a] Marta Blasco-Ahicart,[a] Miguel García-Tecedor,[b] Mabel de Fez Febré,[a, c] Peng-Yi Tang,[d] Jordi Arbiol,[d, e] Sixto Giménez,[b] José Ramón Galán-Mascarós,[a, e] and Núria López*[a]

Sustainable electrocatalysis of the oxygen evolution reaction (OER) constitutes a major challenge for the realization of green fuels. Oxides based on Ni and Fe in alkaline media have been proposed to avoid using critical raw materials. However, their ill-defined structures under OER conditions make the identification of key descriptors difficult. Here, we have studied Fe–Ni–Zn spinel oxides, with a well-defined crystal structure, as a platform to obtain general understanding on the key contributions. The OER reaches maximum performance when: (i) Zn is present in the Spinel structure, (ii) very dense, equimolar 1 : 1 : 1 stoichiometry sites appear on the surface as they allow the formation of oxygen vacancies where Zn favors pushing the electronic density that is pulled by the octahedral Fe and tetrahedral Ni redox pair lowering the overpotential. Our work proves cooperative electronic effects on surface active sites as key to design optimum OER electrocatalysts.

## Introduction

Our energy needs to keep up with current and future demands worldwide calls for a revolution in the way we harvest, convert and store renewable sources.[1] Water splitting has emerged as a plausible energy harvesting technology as electric energy can drive two redox semi-reactions: oxidation of water at the anode to generate $O_2$ (oxygen evolution reaction, OER), extraction of protons and electrons to generate $H_2$ (hydrogen evolution reaction, HER) at the cathode. The kinetic bottleneck (largest overpotential) appears in the anodic side and the best catalysts $IrO_2$ and $RuO_2$, contain scarce elements which questions their scalability and wide implementation.[2] Therefore, the search for robust and efficient catalysts for the oxygen evolution reaction based on earth-abundant materials poses a major scientific and technical challenge.[3,4]

Nickel (Ni) is an earth-abundant first row-transition metal whose OER catalytic activity was discovered at the beginning of last century.[5] Nowadays, Ni is the principal catalyst component of commercial alkaline water electrolysers.[6–9] Experimental studies demonstrated that the evolving Ni-oxyhydroxide incorporates Fe from the electrolyte,[10] and this Fe-doped Ni material is the genuine highly active OER catalyst.[11–13] Since this cooperative effect was identified, different mixtures in the form of NiFe alloys,[14] NiFe oxides[15] and NiFe layered double hydroxides have been explored. An early extensive combinatorial study with 3500 structures identified that Ni-based (minimum 0.6 ratio) Fe-doped systems could be further enhanced by Sr, Ba, W, Ce, Ga or Mo.[16]

Alternatively, dopants with high potentials for the 2+/3+ redox pair have been proposed theoretically, such as Fe–Cu pairs in NiOOH materials.[17] Ni doping was found to be less effective than Zn-doping on hematite, correlated to the $d^{10}$ close shell of the latter.[18] Studies on rare-earth perovskites[19–21] indicated that activity depends on the $e_g$ occupation. The activity of spinel structures[22–25] has been correlated to vacancy formation energy,[26] center of the p-band of the oxygen O(2p),[26,27] metal occupation,[28] and M–O covalency,[19] although it has been recently identified that asymmetric bulk covalency between two metals can also be used as a descriptor.[4] However, surface composition can divert from the nominal bulk stoichiometries due to segregation and leaching.

This erratic, and even contradictory, catalytic reports for multiple oxide phases, where the same active metal has apparently different effects, has limited rational strategies for further enhancement. The high degree of complexity and phase diversity in many Ni-based catalysts makes it difficult to rationalize structure vs stoichiometry vs cooperative co-dopant effects as they can simultaneously modify: (i) the genuine active phase under OER and (ii) the surface state and/or local coordination. To overcome these limitations we have reverted to a robust structural platform, that of Fe spinel ferrites, as they are stable in aqueous media in a wide pH range. In these

[a] Dr. F. A. Garcés-Pineda, Dr. H. Chuong Nguyën, Dr. M. Blasco-Ahicart, M. de Fez Febré, Prof. J. R. Galán-Mascarós, Prof. N. López
Institute of Chemical Research of Catalonia (ICIQ), The Barcelona Institute of Science and Technology, Av. Països Catalans 16, Tarragona 43007, Spain
E-mail: nlopez@iciq.es
[b] Dr. M. García-Tecedor, Prof. S. Giménez
Institute of Advanced Materials (INAM), Universitat Jaume I, 12006 Castelló, Spain
[c] M. de Fez Febré
Departament de Química Física i Inorgànica, Universitat Rovira i Virgili, Marcel.lí Domingo 1, Tarragona 43007, Spain
[d] Dr. P.-Y. Tang, Prof. J. Arbiol
Catalan Institute of Nanoscience and Nanotechnology (ICN2), CSIC and BIST, Campus UAB, Bellaterra, 08193 Barcelona
[e] Prof. J. Arbiol, Prof. J. R. Galán-Mascarós
Catalan Institution for Research and Advanced Studies (ICREA), Pg. Lluís Companys 23, 08010 Barcelona, Catalonia, Spain

materials two components can be modulated while maintaining its major structural features to rationalize electronic effects on electrocatalytic performance. Spinel type oxides ($AB_2O_4$) have a cubic structure where $B^{3+}$ atoms occupy octahedral sites and $A^{2+}$ ions are placed in tetrahedral positions. This distribution can be switched depending on stoichiometry and preparation, as an excess of divalent $A^{2+}$ favors swapping positions.

In this work, we have taken two compositions as starting materials, the $AFe_2O_n$ ($n \leq 4.0$) and the $A_2FeO_n$ spinel ($n \leq 3.5$), as to analyze the effect of controlled stoichiometry where A=$Ni^{2+}$, $Zn^{2+}$ on their catalytic performance towards OER. By integrating experimental and theoretical techniques, we have found that maximum electrocatalytic OER activity is achieved in the equimolar $ZnNiFeO_n$, rationalized in terms of surface structure and reaction mechanism. We have identified a cooperative electronic effect as responsible for the enhanced reactivity, where all three components help to facilitate the lowest-energy transition pathway allowed due to the synergistic effect among their individual electronic properties, delivering an optimum balance between electronic "push and pull" effects. Our computational model identifies this rich and powerful strategy to improve earth-abundant OER electrocatalysts following this cooperative rationale.

## Results and Discussion

We prepared the two series $Ni_{1-x}Zn_xFe_2O_n$ and $(Ni_{2-x}Zn_x)_2FeO_n$ with variable Zn composition by combustion methods. Their spinel structure was confirmed by powder X-ray diffraction (Figures S1–S7 in the Supporting Information). The compounds were deposited onto Ni substrates as ionomer inks (see Experimental Section) for electrochemical characterization in 0.1 M KOH. Upon anodic linear sweep voltammetry (LSV), all compounds showed an exponential current density increase at $>275$ mV overpotential, associated to the appearance of the catalytic OER event (Figure 1a–c and Figure S8).

Taking the overpotential at 10 mA/cm$^2$ as parameter of interest to compare the activity of these catalysts, the spinel $Ni_{1-x}Zn_xFe_2O_n$ phases needed $>340$ mV overpotential, showing very little dependence on the Zn % content. Actually, the best OER catalysts in this series are those with minimum Zn content, with a small trend towards higher overpotentials as the Zn content increases, reaching overpotentials above 370 mV for Zn = 1.

In contrast, the OER performance of the $(Ni_{2-x}Zn_x)_2FeO_n$ spinels, where Fe content is limited to 33% of the total metal sites (see Figure 1b), follows a completely different dependence on Zn content. The overpotential to reach 10 mA/cm$^2$ presents a volcano shape as a function of Zn % (Figure 1b and Figure S9), reaching maximum activity for the NiZnFe 1:1:1 ($NiZnFeO_n$), showing worse, but almost identical performance for the two pure ($Ni_2FeO_n$) and ($Zn_2FeO_n$) limiting compounds.

To further analyse this different behavior we studied one catalyst from each series $NiFe_2O_n$ and $NiZnFeO_n$ in more detail. Stability tests for these two materials were performed by chronopotentiometric measurements at 10 mA/cm$^2$ for up to 72 h (Figure 2b) without significant degradation. The electrocatalytic evolution with time shows an increase in overpotential of 90 mV for $NiFe_2O_n$, but a continuous improvement for

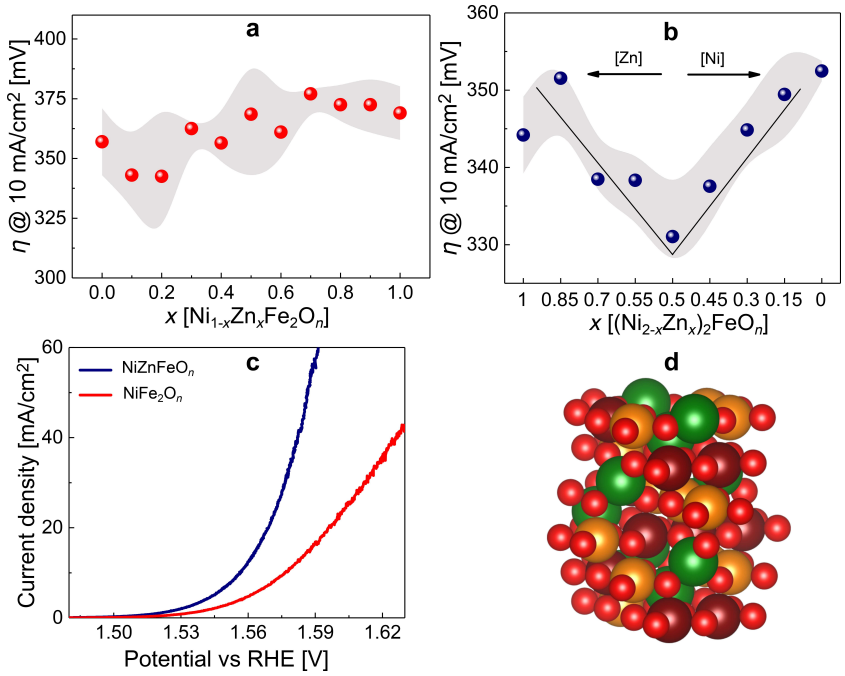


**Figure 1.** Overpotentials at 10 mA/cm$^2$ of the NiZnFe spinels (**a**) stoichiometric, $Ni_{1-x}Zn_xFe_2O_n$ and (**b**) non-stoichiometric, $(Ni_{2-x}Zn_x)_2FeO_n$.The shaded area correspond to the error obtained from ANOVA analysis from several independent experiments. In (**c**) the comparison between both spinels ($NiFe_2O_n$ and $NiZnFeO_n$) with the optimized stoichiometry, supported on Nickel-rotating disk electrode (Ni-RDE) and (**d**) corresponds to the crystalline structure of the spinel. Green spheres stand for Zn, Orange for Ni, Wine represents Fe and Red corresponds to O.

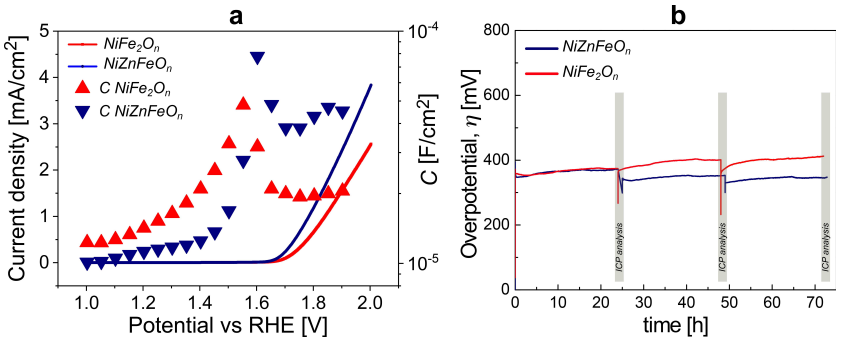


**Figure 2.** (**a**) Capacitances extracted from EIS measurements for both analyzed samples deposited on FTO substrates for the $NiFe_2O_n$ and $NiZnFeO_n$ compounds performed in pH 13 (KOH 0.1 M). (**b**) Potentiometry $NiFe_2O_n$ ferrite and $NiZnFeO_n$ spinel polarized at 10 mA/cm$^2$ during 72 h, using an Ni-RDE electrode. Each 24 h a sample of electrolyte was analysed by ICP technique.

$NiZnFeO_n$, decreasing the initial overpotential by 52 mV. This enhancement under working conditions is also distinct.

XPS spectra of fresh and used electrodes showed no significant differences, supporting the stability of the material during electrocatalytic water splitting (Figures S11, S12). $NiZnFeO_n$ was analysed with high resolution transmission electron microscopy (HRTEM)(Figure 3), before and after 72 h electrolysis. The analysis showed no degradation of the crystalline structure or morphological changes. Chemical composition was also consistent. ICP-MS analysis of the electrolytic solutions recovered after long-term bulk electrolysis (Table S3) detected no Fe nor Ni leaching ($<1\%$), but a $\sim 14\%$ Zn leaching after the 72 h. To better determine the limits of this leaching, we re-used the same electrode for two more 24 h chronopotentiometries, finding 3% and 2% Zn leaching, respectively. This suggest that Zn leaching is only partial, and probably arises from major defects or particular facets, with more than 80% of the initial Zn content remaining in the oxide structure after $>120$ h of continuous OER. This leaching could be related to the electrocatalytic enhancement observed in working conditions, since ion leaching may increase the surface area of the material, facilitating the accessibility of active sites to water molecules.[16]

To better understand the distinct OER activity of $NiZnFeO_n$, we performed electrochemical impedance spectroscopy (EIS) on both electrocatalysts as deposited on FTO substrates. Since a single arc was observed in the Nyquist plots, a simple Randles' equivalent circuit (Figure S9 and S10b) was employed to fit the raw data. The series resistance, $R_s$, mainly related to the substrate conductivity and the wire connections is practically constant, for all the potential values tested: $\sim 36\ \Omega\ cm^2$. On the

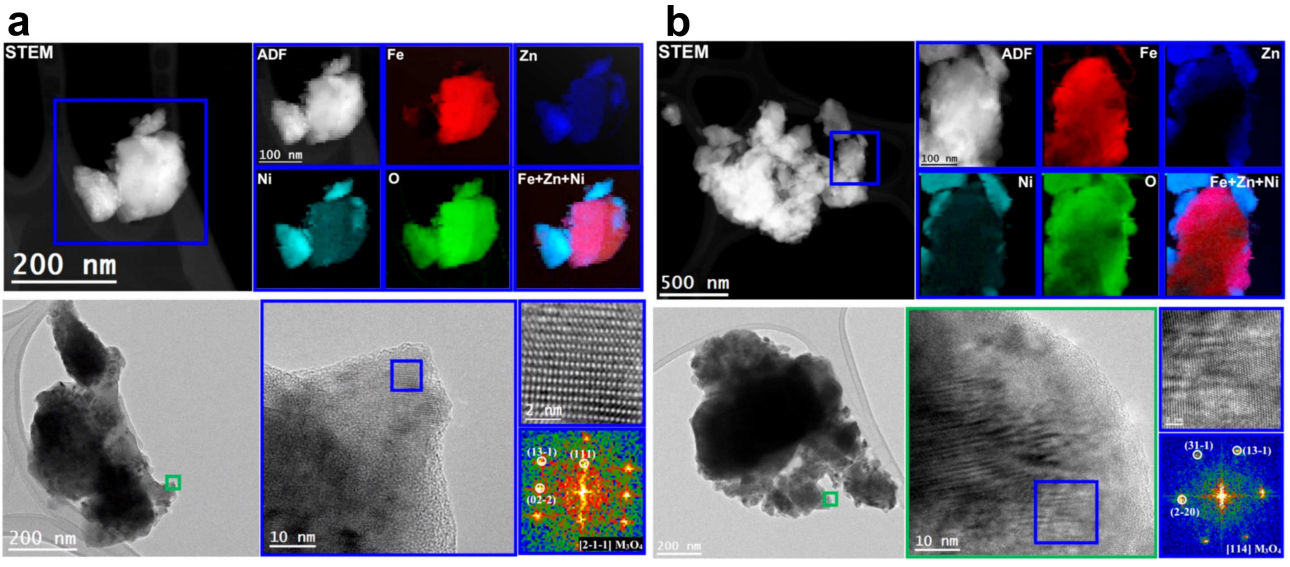


**Figure 3.** STEM characterisation of $NiZnFeO_n$ (**a**) before potentiometry and (**b**) after the electrochemical test: EELS chemical composition maps obtained from the blue rectangle area in the ADF-STEM micrograph. Individual Fe (red), Ni (indigo), Zn (blue), O(green) maps and composite maps. Left and middle: low magnification TEM micrograph shows edge structure of the nanoparticle. Right top: magnified detail TEM of the blue squared region and right bottom: the corresponding temperature colored FFT spectrum, which indicates that it crystallizes in the cubic $M_3O_4$ [*F D3-MZ*]-space group 227, with lattice parameters of $a=b=c=0.8391$ nm/ 0.84068 nm/0.83457 nm, and $\alpha=\beta=\gamma=90$ as visualised along the [2 $\bar{1}$ $\bar{1}$]-/[114] direction.

other hand, the charge transfer resistances ($R_{ct}$) decrease with the applied potential (Figure S10a), in good correspondence with the dc resistance estimated from the *j-V* curve, since $R_{dc} = (dj/dV)^{-1}$. Consequently, a smaller $R_{ct}$ was measured for the spinel with the best performance, $NiZnFeO_n$. At high anodic potentials ($V > 1.7$ $V_{RHE}$) $R_s$ is the limiting resistance for the catalyst performance, which highlights the dramatic effect of the substrate. The extracted capacitances for both samples under study are showed in Figure 2a, while the capacitance of the FTO substrate, as a reference, is shown in Figures S9a and S10. The FTO capacitance shows a constant behavior with the applied potential typical of a double layer capacitance in a metal/liquid or degenerated semiconductor/liquid interface. However, the estimated capacitances associated to the spinels show a clear peak close to the onset of the catalysis that is followed by a decrease in the catalytic region. This capacitive peak can be attributed to the accumulation of electrogenerated holes in the spinels before driving the OER, as it has been previously reported for other Ni-based OER electrocatalysts, where the size of the redox wave identified by cyclic voltammetry was directly associated to the density of catalytic sites.[10,29] The $NiZnFeO_n$ spinel shows a higher capacitive peak compared to $NiFe_2O_n$, which can be attributed to a higher density of states, and hence a higher activity towards OER. The difference in the capacitance is $2.27 \times 10^{-5}$ ($F\,cm^{-2}$), while the difference in energy of these two peaks (x-direction) is 0.04 eV, similar to the changes in the vacancy formation energy for the $Fe_2Ni$, $FeNi_2$ and FeNiZn environments, see Table S6.

We performed a DFT (PBE + U) analysis to understand the reactivity of the $NiZnFeO_n$. The bulk spinel $NiZnFeO_n$ belongs to the 227 group and for a supercell of ($2 \times 2 \times 2$), there would be around 9 billion possibilities to rearrange the Zn, Ni and Fe atoms. Tetrahedral sites in spinel have charges +2 and octahedral sites +3. Putting a Zn atom in a octahedral site and +3 state increased the energy of the system by more than 3 eV compared to other tetrahedral configurations. Assuming then that Zn occupies only the tetrahedral sites, there are 97 non-equivalent configurations to sample. Bulk calculations showed that the most stable structure has the largest lattice constant with the structure seen in Figures S13 and S14. The most active surface is (001), different possible terminations appear from this cut and the lowest surface energy termination was used in the mechanistic investigation.

For oxides, both external surface (adsorbate evolution AEM) and lattice oxygen mechanisms (LOM) can be responsible for OER.[4,13,30–37] As the ferrites can easily loose oxygen we have considered LOM as the major mechanism. The water nucleophilic attack occurs over a lattice oxygen vacancy, LOM-WNA (Figure 4), which consists of 4 steps with the following intermediates (*OH, *O, *OOH) that were calculated on the (001) surface through the computational hydrogen electrode method.[38]

This was done for the $Ni_2FeO_n$ at the optimized lattice (8.3706 Å) constant and also on an extended lattice constant (8.4309 Å) to assess the effect of expansion on the OER. We have observed for the $Ni_2FeO_n$ that changing the lattice size alone changes the OER overpotential from 1.23 V to 0.88 V at 1.23 V vs SHE on a single Ni site.

Our DFT calculations show that LOM-WNA is less costly than OER on metal sites by at least 0.7 eV on the optimal $NiZnFeO_n$ (See Table S5). It should be noted however that LOM-WNA is not always better since it can be very costly to form an O vacancy for the $FeFeNiO_n$, $FeNiNiO_n$, and $ZnNiNiO_n$ compounds in Table S6. The observed geometric restructuring during the OER also support the assumption that O lattice are involved in the OER.

We have analyzed the electronic structures for all the intermediates for the LOM-WNA path, and compiled the results in Table S7.

As the vacancy formation energy was proposed as descriptor for the activity,[28] we calculated this parameter and correlated it with the overpotential. The dependence shows that, while all the systems follow a linear trend, the spinel ZnFeNi with 1:1:1 is a clear outlier (See Figure S15). Inspected

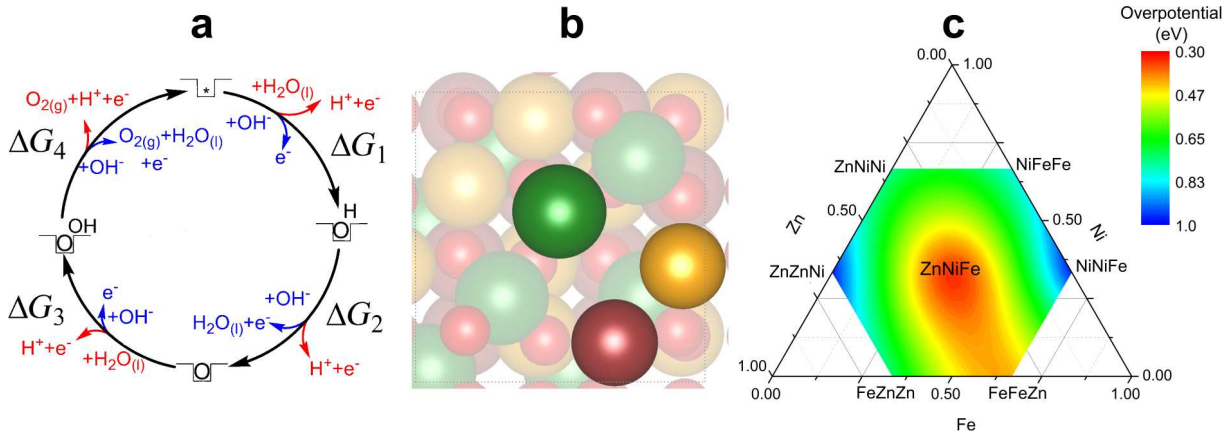


**Figure 4.** (**a**) Proposed catalytic cycle (LOM = Lattice Oxygen Mechanism, WNA = Water Nucleophilic Attack) for $NiZnFeO_n$ occurring at the defective sites, oxygen vacancies of the lattice. (**b**) Top view of the proposed active site with the Zn (green) at the tetrahedral site and Ni (orange) and Fe (red) at the octahedral sites. The lattice oxygen among these three atoms is missing. (**c**) DFT-SHE overpotential for the spinel as a function of the composition fractions Ni, Fe and Zn.

separately Fe surrounded with Zn eases O vacancy formation (step 4) while surrounded by Ni it enhances H release (step 2). Cooperative electronic effects are more difficult to assess as the addition of a new metal alters more than one step in different directions. Bulk assessments like covalency balances are not valid as the activity depends on the particular reaction ensemble.

As for the electronic fine tuning, on $NiZnFeO_n$, Zn behaves as an spectator for each OER step as it has no available redox pair at this potential, but pushes the charge away towards the vacancy. The intermediates thus use the relative $Fe^{3+}/Fe^{4+}$ and $Ni^{2+}$ to $Ni^{3+}$ pairs to fine tune the reactivity. Particularly, Ni lowers step 2 through electron pulling. This step is exceedingly large when Zn is the only constituent species (a more detailed discussion of the magnetization is available in the Supporting Information). Therefore, the cooperative effects through pull-push strategies needed to lead to 1:1:1 composition $NiZnFeO_n$ in the surface ensembles represent the best compromise for all the steps in the cycle.

In comparison the ferrite spinels $NiZnFe_2O_n$, exposed surface ensembles with trimers but in all cases the composition contains two Fe. This leaves only one position available for either Ni or Zn. Therefore no promotion is expected in this case and this is why these materials are not found to improve when Zn is added. Therefore, both the asymmetric covalency of the bonds in the bulk and surface asymmetric sites are crucial to promote OER activity.

In summary, the $NiZnFeO_n$ compound: (i) has the right geometric structure needed for the models to hold ; (ii) has a trimeric Fe–Zn–Ni sites surrounding an $O_{latt}$ in the center that is real OER active site.

## Conclusions

We analyzed the interplay between bulk crystalline phase, surface configuration and electronic structure with catalytic performance for the family of nickel-zinc ferrites, which was initially proposed as a water oxidation electrocatalyst by Stahl et al.[15] Interestingly, stoichiometry modulations did not significantly affect the overall electrocatalytic performance for the spinels, $Ni_{1-x}Zn_xFe_2O_n$. On the contrary, we found a volcano trend in the iron-defective spinel $(Ni_{2-x}Zn_x)_2FeO_n$, reaching optimum performance for the equimolar 1:1:1 Ni:Zn:Fe derivative. The catalytic activity of this cubic spinel was the best in the series, directly competing with the best ternary oxides as reported by Stahl ($\eta_{10\ mA/cm^2} = 325$ mV for $NiFeGaO_n$ and $\eta_{10\ mA/cm^2} = 331$ mV for $NiZnFeO_n$) or those derived from extensive machine learning coupled to experiments $Al_{0.5}Mn_{2.5}O_4$[4] with outstanding stability at high currents. We identified the microscopic origin for this optimum OER electrocatalysts in this series by analyzing the mechanism, and particularly the effects of cation composition at the active site. Our simulations suggest that a push-pull cooperative effects on the oxide surface ensembles, formed by the three different metals are most abundant in the Ni:Zn:Fe spinel and offer the lowest overpotentials, thus predicting its champion behavior. For a potential OER material to be successful, a strict phase and surface orientation control is needed to guarantee that the exposed surface contains the active cooperative ensembles in very dense amounts with a stability that is achieved by employing similar elements. Our combination of experimental evidences with consistent theoretical models opens additional paths for a rational understanding of cooperative effects in electrocatalysis, and for further enhancement of OER electrochemistry.

## Experimental Section

### Catalyst synthesis

All reagents were commercially available and used as received. Mixed metal oxides were prepared by modifying methods available in the literature. Metal nitrates, in the appropriate ratio, were dissolved in 50 mL of distilled water with constant stirring until a clear solution was obtained. The iron concentration was fixed to 0.0125 M and, then, the corresponding amount of each metallic precursor was calculated according to the desired composition. Glycine was added into the aqueous solution (glycine/metal molar ratio = 1.20) and stirred until total dissolution. Afterwards, the solution was heated up to 200 °C until total solvent evaporation and glycine combustion. The resulting porous dark solid was recovered and calcined at 1100 °C in a tubular oven for 1 h. Finally, calcined material was mechanically milled in an Agatha ball milling (2 balls) at 25 Hz for 15 min.

### Electrode preparation

Working electrodes were prepared by drop-casting catalyst-containing inks on the surface of nickel supports. Ni-RDE electrodes (0.07 $cm^2$ surface area) were previously polished with diamond abrasive slurries (DIAPAT-M, 39-321-M, Netkon) in an order of 3 μm and 1 μm diameter particle-based slurries (2 min in each) to obtain mirror surfaces. Synthetic nap based polishing pads (METAPO-B, polishing cloth, self- adhesive back, diamond 3–1 μm, Netkon) were used for diamond polishing. To clean the polished surface, it was sonicated in ethanol for 2 min and air-dried. Catalysts-containing inks were prepared using 10 mg of catalysts, 25.4 μL of 5% (w/w) ionomer solution, 244 μL of water and 732 μL of ethanol. The inks were sonicated for 30 min and then the appropriate volume of ink was drop-casted onto Ni support surfaces to obtain 0.84 mg catalyst/$cm^2$ catalyst loading. The deposited inks were dried in an oven at 60 °C for 5 min.

### Electrochemical measurements

Electrochemical experiments were performed with a Biologic SP-150 potentiostat. The ohmic drop was compensated using the positive feedback compensation implemented in the instrument. All experiments were performed with a three-electrode configuration using 0.1 M KOH (pH 13) as electrolyte solution, employing a graphite rod as counter electrode, a Hg/HgO (NaOH 1 M) reference electrode and catalyst-ink deposited on nickel support as working electrode. Linear sweep voltammetry (LSV) was performed with an ALS RRDE-3 A setup, using a nickel rotating disk electrode (0.07 $cm^2$ surface area) at 1600 rpm. LSV experiments were carried out with a 1 mV/s scan rate. Long-term electrochemical measurements were done in an H-cell where the anode and the cathode compartments were separated by a porous frit and stirred. Bulk measurements

were done under a constant current density of 1 mA/cm$^2$. A 877 Titrino Plus pH-probe (Metrohm) was used to measure the experimental pH for each measurement. The pH value was used to calculate the thermodynamic water oxidation potential ($E^0_{O_2/H_2O}$) by using the Nernst equation:

$$E_{RHE} = E_{Hg/HgO} + 0.059 \times pH + 0.140 \quad (1)$$

considering, $E^0_{NHE} = E_{Hg/HgO} + 0.140$ V for our Hg/HgO (1 M NaOH) reference electrode.

The water oxidation overpotential ($\eta$) was calculated by substracting the thermodynamic water oxidation potential $E^0_{O_2/H_2O} = 1.229$ (V) vs RHE (pH 13) to the experimental potential ($E_{RHE}$) at pH 13.

$$\eta = E_{RHE} - 1.229 \quad (2)$$

### Characterization techniques

Energy-dispersive X-ray spectroscopy (EDX) was collected with a JEOL-JMS6400 environmental scanning electron microscope equipped with an Oxford Instruments X-ray elemental analyser.

Powder X-ray diffraction (powder XRD) data were collected with a Bruker D8 Advance Series equipped with a VANTEC-1 PSD detector.

Raman spectroscopy measurements were acquired using a Renishaw inVia Reflex Raman confocal microscope (Gloucester-Shire, UK), equipped with a diode laser emitting at 514 nm at a nominal power of 300 mW, and a Peltier- cooled CCD detector (−70 °C) coupled to a Leica DM- 2500 microscope. Calibration was carried out daily by recording the Raman spectrum of an internal Si standard. Rayleigh scattered light was appropriately rejected by using edge-type filters. Laser power was used at nominal 10% to avoid sample damage. Spectra were recorded with the accumulation of at least 3 scans with a 30 s scan time each one.

X-ray photoelectron spectroscopy (XPS) used to analyse samples surface was performed at SSTTI University of Alicante. All spectra were collected using Al-K$\alpha$ radiation (1486.6 eV), monochromatized by a twin crystal monochromator, yielding a focused X-ray spot with a diameter of 400 μm, at 3 mA × 12 kV. The alpha hemispherical analyser was operated in the constant energy mode with survey scan pass energies of 200 eV to measure the whole energy band and 50 eV in a narrow scan to selectively measure the particular elements. Charge compensation was achieved with the system flood gun that provides low energy electrons and low energy argon ions from a single source.

Inductively coupled plasma optical emission spectrometry (ICP-OES) was used to carry out elemental analysis with an Agilent 725-ES inductively coupled plasma optical emission spectrometer at University of Valladolid. The basic solution after the electrochemical tests qw collected in a final volume of 50 mL. An aliquot of this basic solution was analysed by ICP-OES.

Electrochemical impedance spectroscopy (EIS) measurements were carried out in three-electrode configuration using a 0.1 M KOH solution (pH 13). The studied electrocatalyst deposited onto an FTO substrate was connected to the working electrode, while a Ag/AgCl (3 M KCl) was used as reference electrode and a Pt wire as a counter electrode. All potentials were referred to the reversible hydrogen electrode (RHE) through the Nernst equation: $V_{RHE} = V_{(Ag/AgCl)} + V^0_{(Ag/AgCl)} + 0.059 \cdot pH$, where $V^0_{(Ag/AgCl)}(3M\ KC1) = 0.21$ V. All experiments were carried out in an AutoLab potentiostat PGSTAT302. The measurements were performed between 0.1 Hz and 1 MHz with 20 mV of amplitude perturbation, with a step potential of 50 mV in the anodic direction. The EIS data were analyzed with the ZView software (Scribner associates).

Scanning transmission electron microscopy (STEM) was done by the Group of Advanced Electron Microscopy in the Institut Català de Nanociència i Nanotecnologia (ICN2) in Barcelona, using a FEI Tecnai F20 field emission gun microscope operated at 200 kV with a point-to-point resolution of 0.19 nm. The samples were dispersed in cyclohexane and collected on TEM copper grids. Compositional analyses were performed by electron energy loss spectroscopy (EELS) with a GATAN Quantum spectrometer coupled to the F20 TEM.

### Computational details

We used Quantum Espresso 6.2[39,40] with USPP from the standard solid-state pseudopotentials (SSSP) library optimized for precision and efficiency.[41] DFT + U the GGA PBE functional[42] was used with the cut-offs set as ecutwfc = 40.0 Ry and ecutrho = 320.0 Ry. The Hubbard terms for PBE + U were set to U(Ni) = 6.2 eV,[43] U(Fe) = 4.2 eV.[44] DFT-D2 dispersion correction were applied with Grimme-D2 parameters.[45] The software made by Dr Ricardo Grau-Crespo[46] was used to sample all the possibilities to rearranged the $NiFeZnO_4$ spinel in a (2 × 2 × 2) supercell with the symmetry space group 227 (Fd-3 m). We computed the energy of the intermediates (*OH, *O, *OOH) for each step using the computational hydrogen rlectrode.[38] Bulk calculations were performed with 3 × 3 × 3 k-points sampling and slab calculations with 3 × 3 × 1. All structures can be accessed on the ioChem-BD database[47] under the following link https://iochem-bd.iciq.es/browse/review-collection/100/24834/c09e28437355013b1ae73bdb.

## Author contribution

F.A. G.-P. and H.-C. N. contributed equally to this work. J.R.G.-M. conceptualized the idea. F.A.G.-P., M. B.-A., M. F.F. performed the synthesis and testing, M. G.-T., S. G. electrochemical analysis, P.-Y. T., J. A. microscopy investigation, H.-C.N. computational studies. J.R.G.-M. and N. L. coordinated the writing with input from all the authors.

## *Acknowledgements*

*This work was funded by the European Union under the H2020 FET-PROACT A-LEAF project (Grant Agreement No. 732840). The authors thankfully acknowledge the computer resources at MareNostrum and the technical support provided by the Barcelona Supercomputing Center (QCM-2018-3-0012 Theoretical studies on catalysis optimization for an Artificial Leaf (A-LEAF)). ICN2 acknowledge funding from Generalitat de Catalunya 2017 SGR 327. ICN2 and UJI acknowledge funding from the Spanish MINECO coordinated project VALPEC (ENE2017-85087-C3). ICN2 is supported by the Severo Ochoa program from Spanish MINECO (Grant No. SEV-2017-0706) and is funded by the CERCA Programme / Generalitat de Catalunya.*

## *Conflict of Interest*

The authors declare no conflict of interest.

**Keywords:** mixed metal oxides · spinels · oxygen vacancy · water splitting · descriptors

[1] R. J. Detz, J. N. H. Reek, B. C. C. van der Zwaan, *Energy Environ. Sci.* **2018**, *11*, 1653–1669.
[2] K. Sardar, E. Petrucco, C. I. Hiley, J. D. Sharman, P. P. Wells, A. E. Russell, R. J. Kashtiban, J. Sloan, R. I. Walton, *Angew. Chem. Int. Ed.* **2014**, *126*, 11140–11144.
[3] B. M. Hunter, H. B. Gray, A. M. Müller, *Chem. Rev.* **2016**, *116*, 14120–14136.
[4] Y. Sun, H. Liao, J. Wang, B. Chen, S. Sun, S. J. H. Ong, S. Xi, C. Diao, Y. Du, J.-o. Wang, M. B. H. Breese, S. Li, H. Zhang, Z. J. Xu, *Nat. Catal.* **2020**, https://doi.org/10.1038/s41929–020–0465–6.
[5] A. Coehn, M. Gläser, *Z. Anorg. Chem.* **1902**, *33*, 9–24.
[6] J. D. Holladay, J. Hu, D. L. King, Y. Wang, *Catal. Today* **2009**, *139*, 244–260.
[7] T. Metall, D. E. Hall, *J. Electrochem. Soc.* **1981**, 740–746.
[8] C. T. Bowen, H. J. Davis, B. F. Henshaw, R. Lachance, R. L. LeRoy, R. Renaud, *Int. J. Hydrogen Energy* **1984**, *9*, 59–66.
[9] M. B. Janjua, R. L. Le Roy, *Int. J. Hydrogen Energy* **1985**, *10*, 11–19.
[10] L. Trotochaud, S. L. Young, J. K. Ranney, S. W. Boettcher, *J. Am. Chem. Soc.* **2014**, *136*, 6744–6753.
[11] M. Gong, H. Dai, *Nano Res.* **2015**, *8*, 23–39.
[12] S. Lee, K. Banjac, M. Lingenfelder, X. Hu, *Angew. Chem. Int. Ed.* **2019**, *58*, 10295–10299.
[13] Y. Zhou, N. Lopez, *ACS Catal.* **2020**, *10*, 6254–6261.
[14] Y. Ullal, A. C. Hegde, *Int. J. Hydrogen Energy* **2014**, *39*, 10485–10492.
[15] J. B. Gerken, J. Y. Chen, R. C. Massé, A. B. Powell, S. S. Stahl, *Angew. Chem. Int. Ed.* **2012**, *51*, 6676–6680; *Angew. Chem.* **2012**, *124*, 6780–6784.
[16] J. B. Gerken, S. E. Shaner, R. C. Massé, N. J. Porubsky, S. S. Stahl, *Energy Environ. Sci.* **2014**, *7*, 2376–2382.
[17] J. M. P. Martirez, E. A. Carter, *ACS Energy Lett.* **2020**, *5*, 962–967.
[18] H. C. Nguyën, F. A. Garcés-Pineda, M. de Fez-Febré, J. R. Galán-Mascarós, N. López, *Chem. Sci.* **2020**, *11*, 2464–2471.
[19] A. Grimaud, O. Diaz-Morales, B. Han, et al, *Nat. Chem.* **2017**, *9*, 457.
[20] W. Xie, Y.-L. Lee, Y. Shao-Horn, D. Morgan, *J. Phys. Chem. Lett.* **2016**, *7*, 1939–1944.
[21] Y.-L. Lee, D. Lee, X. R. Wang, H. N. Lee, D. Morgan, Y. Shao-Horn, *J. Phys. Chem. Lett.* **2016**, *7*, 244–249.
[22] Q. Zhao, Z. Yan, C. Chen, J. Chen, *Chem. Rev.* **2017**, *117*, 10121–10211.
[23] J. Y. C. Chen, J. T. Miller, J. B. Gerken, S. S. Stahl, *Energy Environ. Sci.* **2014**, *7*, 1382–1386.
[24] Y. Zhou, S. Sun, J. Song, S. Xi, B. Chen, Y. Du, A. C. Fisher, F. Cheng, X. Wang, H. Zhang, Z. J. Xu, *Adv. Mater.* **2018**, *30*, e1802912.
[25] Y. Duan, S. Sun, Y. Sun, S. Xi, X. Chi, Q. Zhang, X. Ren, J. Wang, S. J. H. Ong, Y. Du, L. Gu, A. Grimaud, Z. J. Xu, *Adv. Mater.* **2019**, *31*, 1807898.
[26] Y.-L. Lee, J. Kleis, J. Rossmeisl, Y. Shao-Horn, D. Morgan, *Energy Environ. Sci.* **2011**, *4*, 3966–3970.
[27] A. Grimaud, K. J. May, C. E. Carlton, Y.-L. Lee, M. Risch, W. T. Hong, J. Zhou, Y. Shao-Horn, *Nat. Commun.* **2013**, *4*, 2439.
[28] J. Suntivich, K. J. May, H. A. Gasteiger, J. B. Goodenough, Y. Shao-Horn, *Science* **2011**, *334*, 1383–1385.
[29] S. Corby, M.-G. Tecedor, S. Tengeler, C. Steinert, B. Moss, C. A. Mesa, H. F. Heiba, A. A. Wilson, B. Kaiser, W. Jaegermann, L. Francàs, S. Gimenez, J. R. Durrant, *Sustain. Energy Fuels* **2020**, https://doi.org/10.1039/D0SE00977F.
[30] Q. Xie, Z. Cai, P. Li, D. Zhou, Y. Bi, X. Xiong, E. Hu, Y. Li, Y. Kuang, X. Sun, *Nano Res.* **2018**, *11*, 4524–4534.
[31] Y. Tong, H. Mao, Y. Xu, J. Liu, *Inorg. Chem. Front.* **2019**, *6*, 2055–2060.
[32] Q. Kang-Wen, C. Xi, Y. Zhang, R. Zhang, Z. Li, G.-R. Sheng, H. Liu, C.-K. Dong, Y.-J. Chen, X.-W. Du, *Chem. Commun.* **2019**, *55*, 8579–8582.
[33] X. Gu, H. Jing, X. Mu, H. Yang, Q. Zhou, S. Yan, S. Liu, C. Chen, *J. Alloys Compd.* **2020**, *814*, 152274.
[34] Z. Jakub, J. Hulva, F. Mirabella, F. Kraushofer, M. Meier, R. Bliem, U. Diebold, G. S. Parkinson, *J. Phys. Chem. C* **2019**, *123*, 15038–15045.
[35] Z.-F. Huang, J. Song, Y. Du, S. Xi, S. Dou, J. M. V. Nsanzimana, C. Wang, Z. J. Xu, X. Wang, *Nat. Energy* **2019**, *4*, 329–338.
[36] S. Y. Lim, S. Park, S. W. Im, H. Ha, H. Seo, K. T. Nam, *ACS Catal.* **2020**, *10*, 235–244.
[37] L. Zhang, Q. Fan, K. Li, S. Zhang, X. Ma, *Sustain. Energy Fuels* **2020**, *4*, 5417–5432.
[38] J. K. Nørskov, J. Rossmeisl, A. Logadottir, L. Lindqvist, J. R. Kitchin, T. Bligaard, H. Jónsson, *J. Phys. Chem. B* **2004**, *108*, 17886–17892.
[39] P. Giannozzi, et al., *J. Phys. Condens. Matter* **2017**, *29*, 465901.
[40] P. Giannozzi, et al., *J. Phys. Condens. Matter* **2009**, *21*, 395502.
[41] G. Prandini, A. Marrazzo, I. E. Castelli, N. Mounet, N. Marzari, *npj Comput. Mater.* **2018**, *4*, 72.
[42] J. P. Perdew, K. Burke, M. Ernzerhof, *Phys. Rev. Lett.* **1996**, *77*, 3865–3868.
[43] S. L. Dudarev, G. A. Botton, S. Y. Savrasov, C. J. Humphreys, A. P. Sutton, *Phys. Rev. B* **1998**, *57*, 1505–1509.
[44] M.-T. Nguyen, N. Seriani, S. Piccinin, R. Gebauer, *J. Chem. Phys.* **2014**, *140*, 064703.
[45] S. Grimme, *J. Comput. Chem.* **2006**, *27*, 1787–1799.
[46] R. Grau-Crespo, S. Hamad, C. R. A. Catlow, N. H. De Leeuw, *J. Phys. Condens. Matter* **2007**, *19*, 256201.
[47] M. Álvarez-Moreno, C. de Graaf, N. López, F. Maseras, J. M. Poblet, C. Bo, *J. Chem. Inf. Model.* **2015**, *55*, 95–103.

**Controlling activity by doping**: Earth-abundant materials, typically iron oxide phases (spinels) show only a moderate performance in basic media. In this report, with synergy between theory and experimental work, we demonstrate high performance of Zn,Ni-doped ferrite, proving that cooperative electronic effects at surface- and active-sites are key to designing outstanding OER catalyst.

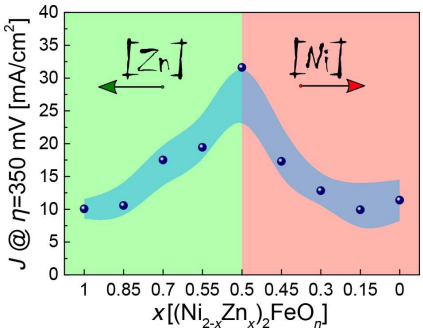


*Dr. F. A. Garcés-Pineda, Dr. H. Chuong Nguyën, Dr. M. Blasco-Ahicart, Dr. M. García-Tecedor, M. de Fez Febré, Dr. P.-Y. Tang, Prof. J. Arbiol, Prof. S. Giménez, Prof. J. R. Galán-Mascarós, Prof. N. López**

1 – 8

**Push-Pull Electronic Effects in Surface-Active Sites Enhance Electrocatalytic Oxygen Evolution on Transition Metal Oxides**